Under consideration for publication in
International Journal of Aeroacoustics

On the use of the Ffowcs Williams-Hawkings equation to predict far-field jet noise from large-eddy simulations

By S. Mendez†, M. Shoeybi, S. K. Lele and P. Moin

Center for Turbulence Research,
Stanford University, Stanford, CA, 94305, USA

ABSTRACT

This study presents best practices for the use of the permeable-surface Ffowcs Williams-Hawkings equations to calculate far-field sound from large-eddy simulations of high-speed turbulent jets. A parametric study of the Ffowcs Williams-Hawkings equations is performed by post-processing existing large-eddy simulations at different operating conditions gathering subsonic, supersonic, cold, isothermal, and heated jets. It is concluded that using the pressure formulations of the Ffowcs Williams-Hawkings equations yields better results than the density formulation, especially for the heated jet. In terms of surface closure, best results are obtained with closed surfaces, in conjunction with outflow disk averaging, which confirms the results obtained by Spalart and Shur in 2009. This is different from most previous studies, which recommend using open surfaces. In addition, detailed implementation information and quantified technical recommendations are presented as a guideline for post-processing large-eddy simulations for jet noise.

1. MOTIVATION AND OBJECTIVES

Despite 60 years of active research on jet noise, the noise generated by expulsion of hot gases at the exhaust of aircraft engines remains an important part of aircraft noise. To assist the experimental efforts in finding innovative solutions for jet noise reduction, numerical methods have been developed during the last decades. Among them, Large-Eddy Simulation (LES) has the potential to become a tool of choice to perform predictions of the noise generated by turbulent jets [1].

One of the main outputs of interest in jet noise simulations is the far-field noise. In recent jet-noise LES, far-field sound predictions are presented for observer angles from 20° to 160° (though results for angle lower than 50° are rarely presented). Development in computer resources now enable sound predictions for frequencies over approximately two decades. The highest resolved Strouhal number varies depending on the operating point and grid refinement, but typical values are about 2 to 5 [1–8]. Note that in practice, far-field sound is not directly obtained from the LES: while LES is well suited for the computation of the turbulent flow, it would be inefficient and inaccurate to use the full LES equations to propagate acoustic waves to the far field. Alternatively, one can compute the far-field sound by directly propagating the near pressure fluctuations to the far field

† Corresponding author: Simon Mendez (smendez@um2.fr), Now in University Montpellier II. I3M, UMR CNRS 5149.

by solving the Euler equations [2] or the linear acoustic equations [3]. Although these methods are far less expensive than LES, they still require additional 3D computational grids and far-field boundary conditions. One can also rely on acoustic analogies, such as the Lighthill analogy [9–11] or Goldstein's generalized acoustic analogy [4, 12], which allow the computation of the far-field sound from the modeling of noise sources.

Surface integral methods such as Kirchhoff [13] or Ffowcs Williams-Hawkings (FWH) [14] methods (with volumetric source terms, corresponding to the presence of quadrupoles outside the surface, neglected) rely on near-field information gathered over a surface enclosing as much as possible the noise sources. The latter methods, owing to their simplicity, their limited cost and their success (when coupled with LES) in predicting the noise emitted by high-speed jets, are very popular in the jet noise LES community [5, 8, 11, 15–20]. The FWH method is generally preferred over the Kirchhoff method: Kirchhoff methods provide accurate results when the surface is placed in the linear acoustic region, which forces the LES grid to be fine even outside of the turbulent region [5, 11, 21].

In an effort to develop a numerical framework using LES for jet noise predictions [6, 22], a FWH solver is implemented. However, despite numerous studies published, no consensus emerges from the literature on how to implement and use a permeable-surface FWH solver. First, practical issues are rarely discussed. Moreover, important discrepancies exist in the literature regarding fundamental issues as the formulation of the equation and the definition of the FWH surface. The question of the treatment of the downstream end of the FWH surface is a prime example of the type of debates related to the use of a FWH solver. When closed surfaces are used, spurious noise is generated by the passage of turbulent eddies through the downstream end, which is compensated by the volume term in the exact FWH integration. Thus, using open surfaces at the downstream end would reduce the error related to the omission of this volume term. However, open surfaces introduce their own errors: data is not recorded on a portion of the surface and more importantly, truncation of the surface generates artificial spurious noise. The question of which errors spoil the results most is not resolved. Articles often conclude that open surfaces yield better results than closed surfaces [among others 11, 15, 16]. On the contrary, Shur *et al.* [17] argue that using open surfaces is arbitrary, and leads to a loss of information at shallow downstream angles. Moreover, they show that truncated surfaces provide highly inaccurate predictions at low frequencies, due to the generation of 'pseudo sound'.

The objective of the present paper is to provide a parametric study in order to obtain best practices for the use of FWH solvers for jet noise applications. Far-field noise is computed from existing turbulent jet LES databases gathering different operating conditions (subsonic and supersonic, isothermal, cold or heated jets) [6, 22]. The tested options include the data windowing, the FWH equation formulation and the downstream end closure. In section 2, the numerical procedure for the sound computation is reported. As implementation itself may have its importance, the technical implementation is more detailed than in most publications. After presenting the LES database in section 3, results are displayed and analyzed in section 4. Section 5 is dedicated to the definition of best practices for using FWH solvers, summarizing the conclusions of the preceding results.

2. NUMERICAL METHOD

2.1. FWH solver

This section describes the procedure employed to calculate the far-field sound. The reader is referred to the detailed paper by di Francescantonio (1997) [21] for the derivation of the FWH equation. The time history of conservative variables is saved over a given surface S (referred to as FWH surface, and detailed in next section) at a specified sampling frequency f and for a total time τ. f is associated with the Nyquist Strouhal number $St_{max} = fD/2U_j$, where $D = 2R$ is the nozzle diameter at the exit (R the radius) and U_j is the jet velocity at the nozzle exit. τ determines the minimum frequency accessible by this post-processing $St_{min} = D/\tau U_j$.

For each surface element of S, the time history of source terms F_1 and F_2 are constructed from the conservative variables using the following expressions:

$$F_1 = \frac{p'\hat{n}_j\hat{r}_j + \rho u_j u_n \hat{r}_j}{c_0 r} + \frac{\rho u_n}{r} \qquad \text{and} \qquad F_2 = \frac{p'\hat{n}_j\hat{r}_j + \rho u_j u_n \hat{r}_j}{r^2}. \tag{1}$$

$\hat{n}_j$ is the jth component of the unit surface normal vector, and $r\hat{r}_j$ represents magnitude and direction of the vector from the surface element location $\mathbf{y}$ to the observer location $\mathbf{x}$. In the expression of F_1 and F_2, p' is the fluctuating pressure ($p' = p - p_\infty$, where subscript ∞ refers to the ambient value), u_j is the jth component of the velocity vector, and $u_n = u_i\,\hat{n}_i$. Note that the effect of viscous stresses has been neglected. In the original formulation [14], ρ is the density. Alternatively, for far-field sound computations in the absence of volume integral, two pressure-based formulations are proposed [5, 23], replacing ρ in Eq. (1) either by $\rho^* = \rho_\infty + p'/{c_\infty}^2$ or by $\rho^\diamond = \rho_\infty\,(p/p_\infty)^{1/\gamma}$. Tests performed on the present LES databases confirmed the findings of the earlier studies [5, 23] that the narrowband sound pressure levels for the two formulations barely differ (by less than 0.01 dB for all angles and frequencies). Thus, no distinction is made between these two formulations in the rest of this paper.

After subtracting the mean, F_1 and F_2 are windowed using a Hanning window [24] and time-Fourier-transformed. The time derivative of F_1 is calculated in the frequency space. The retarded time ($exp(-i\omega r/c_\infty)$) is also applied in the frequency space. The integral of the source terms over the surface then yields the Fourier transform of the pressure at the observer location (with the Fourier transform of g, $\hat{g}(\omega) = \int_{-\infty}^{\infty} g(t)e^{-i\omega t}dt$):

$$4\pi\hat{p}(\mathbf{x},\omega) = \int_S i\omega\,\hat{F}_1(\mathbf{y},\omega)exp(-i\omega r/c_\infty)d\mathbf{y} + \int_S \hat{F}_2(\mathbf{y},\omega)exp(-i\omega r/c_\infty)d\mathbf{y}. \tag{2}$$

Note that $\mathbf{y}$ is the barycenter of surface element dS.

The Narrowband Sound Pressure Level (SPL) level (in dB) is calculated as:

$$SPL(\mathbf{x}, St) = 10\,log_{10}\left(\frac{2\,\hat{p}(\mathbf{x},\omega)\hat{p}^*(\mathbf{x},\omega)}{St_{min}\,p_{ref}^2}\right), \tag{3}$$

where $\hat{p}^*$ is the complex conjugate of $\hat{p}$, $p_{ref} = 2 \times 10^{-5}$ Pa and $St = \omega D/2\pi U_j$. The observer angle θ is defined from the jet axis, pointing upstream (see Fig. 1). Jets considered in the present study are axisymmetric and azimuthal averaging is used to obtain better statistical convergence: for each value of θ, power spectral densities are calculated at 64 azimuthal locations and averaged.

The Overall Sound Pressure Level ($OASPL$, in dB) is calculated as

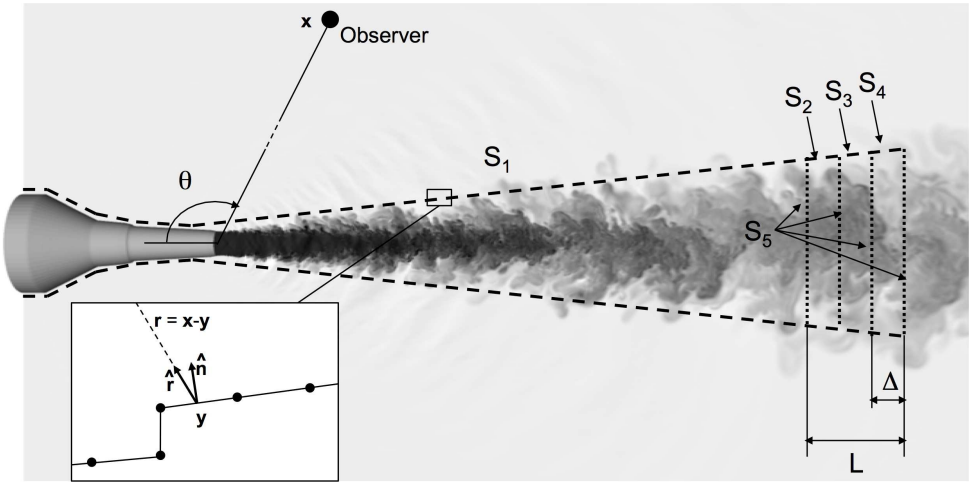

FIGURE 1. Example of a FWH surface when outflow disk averaging is used; the surface is superimposed over an instantaneous LES density field. Inset: zoom on the surface elements of the FWH surface and definition of geometrical quantities used in Eqs. (1) and (2). Dots and lines represent grid vertices and faces used to define the FWH surface elements for integration.

$$OASPL(\mathbf{x}) = 10\,log_{10}\left(\sum_{St=St_{min}}^{St_{max}} \frac{2\,\hat{p}(\mathbf{x},\omega)\hat{p}^*(\mathbf{x},\omega)}{p_{ref}^2}\right) \tag{4}$$

2.2. FWH surface

Figure 1 shows a typical FWH surface superimposed on a jet instantaneous solution. The FWH surface is the union of several sub-surfaces: the first one, S_1, is defined by a relation $r/D = \mathscr{R}(x/D)$. $\mathscr{R}$ is such that the nozzle geometry (included in the calculation) is inside the surface. Because the grid stretches in the radial direction, the surface must be as close as possible to the jet, but far enough from the axis to include all the major source terms. In the present study $\mathscr{R}$ is a piecewise linear function designed to satisfy as much as possible these two criteria. $\mathscr{R}$ does not necessarily follow the grid lines: the exact surface is the union of the mesh faces that separate the cells cut by the prescribed surface from the cells entirely included inside. The surface elements over which the integration of Eq. (2) is performed are thus LES grid faces. On each surface element, F_1 and F_2 are computed from Eq. (1). In Eq. (1), flow quantities are face-averaged: they are obtained by averaging the nodal values, calculated by the LES, at the four vertices of each grid face. $\hat{n}_j$ is the unit grid face vector and the surface element location $\mathbf{y}$ is the barycenter of the grid face (see the inset in Fig. 1).

Using a FWH integration without volumetric integration is only exact when all the noise sources are included inside the surface. This may be achieved radially by adjusting $\mathscr{R}$, but not at the downstream end, where spurious noise is thus generated. Three different options for the downstream end treatment are compared. If $S = S_1$, then the surface is 'open' at its downstream end. If one outflow disk is included, the surface is then called 'closed'. Technically, all surfaces used are then open at the inflow, but this has no consequence on the calculated sound. In the following, 'closed' surface and 'open' surface refer to the fact that the outflow disk is included or excluded from the FWH surface.

A third option is considered: averaging over outflow disks. This technique was first

used by Shur *et al.* [17]. Results from closed surfaces were substantially improved, in particular at upstream angles, where the amplitude of the physical noise is not sufficient to mask the spurious noise related to the outflow disk. It consists in computing $\hat{p}$ using Eq. (2) for several surfaces having the same $\mathscr{R}$, but an outflow disk located at different axial locations. Results in $\hat{p}$ from the different surfaces are then averaged, canceling the spurious noise generated by the passage of turbulent eddies through the outflow disk, which is not consistent from one surface to another.

The outflow disks will be regularly spaced. The spacing between two consecutive outflow disks is denoted by Δ, and the distance between the first and the last outflow disks is denoted by L. To minimize the amount of data stored, outflow disk averaging is realized by using a single surface, as the one shown by Fig. 1, with different weightings for the different parts of the surface: Eq. (2) is modified:

$$4\pi\hat{p}(\mathbf{x},\omega) = \int_S \left(i\omega\ \hat{F}_1(\mathbf{y},\omega) + \hat{F}_2(\mathbf{y},\omega) \right) exp(-i\omega r/c_\infty)\Psi(\mathbf{y})dS, \tag{5}$$

where $\Psi(\mathbf{y})$ is a weight function depending on the sub-surface. Based on number of disks, this weight function can be easily computed for different regions of surface S. For a surface with n outflow disks, S is composed by $n+1$ sub-surfaces, S_1 being the radial surface before the first outflow disk, S_{n+1} the union of all the outflow disks, and S_i $(i = 2, \cdots, n)$ the radial surface between the (i-1)th and the (i)th outflow disks. Figure 1 shows an example with 4 disks, with the definition of sub-surfaces $S_1, \cdots, S_5$. Ψ is then defined as:

$$\Psi(\mathbf{y} \in S_i) = \begin{cases} \frac{n+1-i}{n} & i \in \{1, \cdots, n\} \\ \frac{1}{n} & i = n+1 \end{cases}. \tag{6}$$

Therefore, by using the proposed method, the FWH solver does not require any modification when outflow disk averaging is involved. Instead, the surface element areas are modified with the weight function given by Eq. (6) in a preprocessing step.

2.3. Numerical method for the large-eddy simulations

The FWH solver is used to post-process an existing LES database. As the focus is not on the LES themselves, only a short presentation of the numerical method used to generate the LES database is given. LES are performed using a compressible version of the unstructured solver CDP, CDP-C [25]. CDP-C is a second-order finite volume solver, with a hybrid implicit-explicit time advancement scheme. Small-scale turbulence is modeled using a Smagorinsky model with the dynamic modeling procedure of Moin *et al.* [26] with Lilly's modification [27]. The artificial bulk viscosity method [22, 28, 29] in a generalized form is used to capture shock waves on unstructured grids. More details about the solver and the LES themselves are presented in previous publications [6, 22, 25].

3. LES DATA SETS AND SOUND EXTRACTION

Three different large-eddy simulations will be used in this report: their main characteristics are displayed in Table 1. Two supersonic jets are considered: simulation S1 focuses on an unheated jet and S2 on a heated jet. S3 is a cold subsonic jet. Unstructured hexahedral meshes are used. The number of grid cells (approximately 16 million) is moderate, but sufficient for the study of the FWH solver.

FWH acoustic calculations are performed using the time record $\tau c_\infty/R$ specified in Table 1, windowed by a Hanning window. When compared to experimental data, noise

Simulation	M_j	M_a	M_∞	TR	Re_j	Grid size	$\Delta t c_\infty/R$	$\tau c_\infty/R$	St_{min}	St_{max}
S1	1.39	1.39	0.008	1.0	150,000	17×10^6	0.005	360	0.004	7.2
S2	1.39	1.84	0.008	1.76	76,600	17×10^6	0.005	360	0.003	5.4
S3	0.97	0.89	0.006	0.84	130,000	15.5×10^6	0.005	250	0.0089	11.2

TABLE 1. Operating conditions and numerical characteristics of the simulations performed. Subscripts j and ∞ refer to the jet at the nozzle exit and the ambient free-stream, respectively. Notations are the following: $M_j = U_j/c_j$, $M_a = U_j/c_\infty$, $M_\infty = U_\infty/c_\infty$, $TR = T_j/T_\infty$, $Re_j = \rho_j U_j D / \mu_j$ (μ_j is the dynamic viscosity at the nozzle exit). $\Delta t c_\infty/R$ is the time step and $\tau c_\infty/R$ the total time used for post-processing.

results for $St < 10\,St_{min}$ are not displayed in the figures, as they have been shown to be insufficiently converged in time [24]. Results are compared with experimental data provided by Dr Bridges [30]. As in the experiment, sound at $100\,D$ is calculated with observers located at $50\,D$ from the nozzle exit and rescaled using the assumption that the amplitude of acoustic waves decays like the inverse of the distance from the nozzle exit. A pressure-based formulation is used by default (except in section 4.3, dedicated to the comparisons between formulations).

The FWH surface first follows the external nozzle shape, then radially extends following:

$$\mathscr{R}(x/D) = 0.75 + 0.1(x/D), \tag{7}$$

for S1 and S2. For the subsonic case S3, a piecewise linear function is imposed for $\mathscr{R}$:

$$\mathscr{R}(x/D) = \begin{cases} 0.55 + 0.0665(x/D) & x/D \leq 2.5 \\ 0.8825 + 0.0337(x/D - 2.5) & 2.5 < x/D \leq 10 \\ 1.388 + 0.0206(x/D - 10) & 10 < x/D \leq 14 \\ 1.503 + 0.0045(x/D - 14) & 14 < x/D \leq x_{end}. \end{cases} \tag{8}$$

As seen in Fig. 1, the FWH surface follows the radial growth of the jet, but is rarely crossed by vortical eddies. Downstream, the surface ends at a prescribed axial location, either by one or several outflow disks, located between $x = 25\,D$ and $x = 32.5\,D$, depending on the cases. When outflow disk averaging is used, the first outflow disk is always located at $x = 25\,D$, with additional parameters Δ and L describing the surface.

Effect of the surface radial location is discussed in Appendix. Mendez et al. [6] compared the directly computed noise for observers located in the LES computational domain with the ones calculated from the present FWH formulation. For low frequencies, results are identical. However, for high frequencies, the noise extracted from the LES drops rapidly due to lack of grid resolution, as the grid stretches radially before reaching the lateral boundaries. In the same way, placing the FWH surface far from the jet axis leads to a loss of information at high frequencies, as the grid cut-off frequency decreases with the radial distance. Therefore, a less aggressive grid stretching in the radial direction near the main jet is recommended in order to have flexibility on choosing a surface that

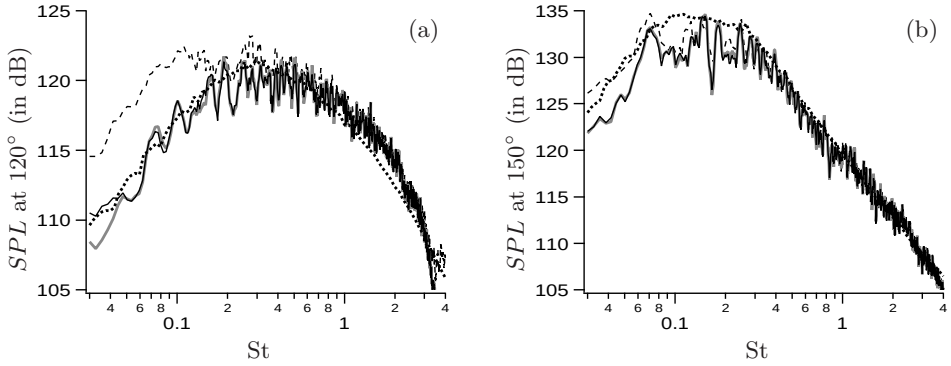

FIGURE 2. Sound pressure level at 120° (a) and 150° (b) for simulation S2 calculated with three different windowing procedures: no windowing (– – – –), hyperbolic tangent windowing (———), and Hanning windowing (═══). Experimental results are also displayed (▪▪▪▪▪).

encloses noise-generating structures as much as possible. Finer grid results are shown in ref. [6].

4. RESULTS

Results obtained using different options are compared in the following sections. Unless otherwise specified, the default options are the following: a pressure-based formulation of the FWH equation is used, from Hanning-windowed data recorded over a surface closed by one outflow disk located at $x_{end} = 25\,D$.

4.1. Windowing

To avoid spectral leakage, signals are windowed before post-processing and then rescaled to conserve the energy of the signal. Figure 2 compares results without windowing, results using a hyperbolic tangent (HT) type window, or using a Hanning window. Window functions using hyperbolic tangent have been used before to maximize the time record effectively taken into account [10, 31]. Sound spectra presented in Fig. 2 show that windowing is necessary. HT and Hanning windows give very similar results, except at low frequencies, where Hanning window gives slightly lower sound. However, the range of frequencies where HT and Hanning windowed results differ is limited. In the following, Hanning window is systematically used.

4.2. Observer distance

In the formulation of the FWH equation employed here, no far-field assumption has been made. Acoustic results thus depend on the distance of the observer to the nozzle exit. This dependance is addressed by computing the acoustic far-field at different observer distances and rescaling them using the r^{-1} decay of acoustic waves to obtain the acoustic far-field at $100\,D$. Note that experimental results are obtained by measuring the acoustic field at $50\,D$ and projecting it to $100\,D$. Figure 3(a) shows the acoustic far-field at $100\,D$. Zooms for upstream and downstream angles are displayed in Fig. 3(b) and 3(c), respectively. Overall sound pressure level is presented rescaling results calculated at $50\,D$ (as in the experiment), $100\,D$, and $125\,D$. $50\,D$ is not sufficient to be in the region where acoustic waves decay as r^{-1}. On the contrary, results calculated at $100\,D$ and $125\,D$ are

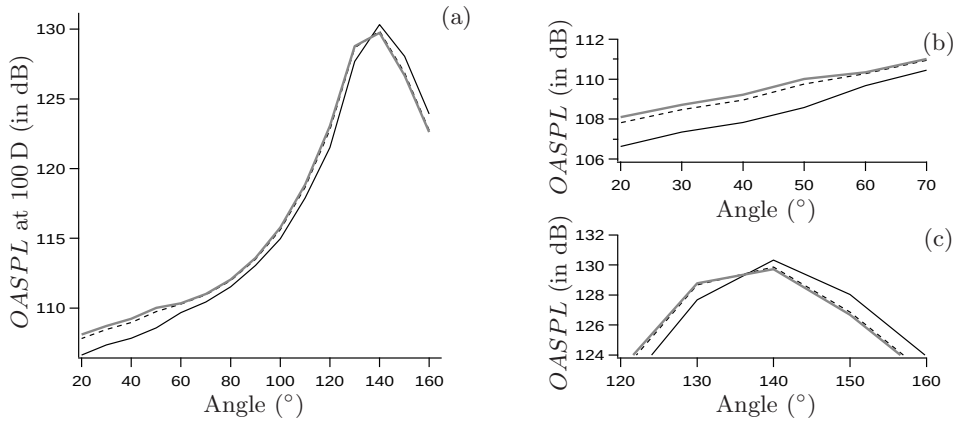

FIGURE 3. Overall sound pressure level for simulation S2 calculated at three different observer distances (a), $50\,D$ (———), $100\,D$ (– – – –), and $125\,D$ (———), and rescaled at $100\,D$. They are calculated at $50\,D$ and rescaled. Subfigures (b) and (c) display zooms at upstream and downstream angles, respectively.

very close. A consequence of this figure is that results will be calculated at $50\,D$ and rescaled to match the experimental procedure.

Some authors use far-field approximations of the FWH equation, with the F_2 term (Eq. 1) omitted [17]. In the present study, sound is calculated at $50\,D$, which is not the true far field. Neglecting F_2 has a substantial impact for low frequencies, but the present time record fails to provide time-converged data anyhow. For the time-converged frequency range, the impact of such an approximation is found to be small but not negligible (less than 1 dB for all observer angles and $St > 0.03$, for S2). The full formulation of the FWH equation is employed in the rest of the study.

4.3. Formulation of the FWH equation

Spalart and Shur [5] have shown that the pressure forms of the FWH equation (section 2) are more forgiving than the original density form, when the FWH equation is solved neglecting the quadrupole term. They show that quadrupole term in the FWH equation is more compact in the pressure formulations. As a consequence, the error made by neglecting it is lower. They also argue that the density formulation is not well suited to situations where important entropy fluctuations cross the FWH surface: in that case, density fluctuations ρ' significantly differ from their acoustic estimation from pressure fluctuations. Using a pressure-based formulation is thus expected to improve results, particularly for hot jets.

Density and pressure formulations are first compared in the case of an unheated jet, the outflow disk of the FWH surface being included (Fig. 4). Sound spectra are very close, consistently with expected low entropy fluctuations. The same observation was made for heated jets when the outflow disk was excluded from the computation (not shown): differences between ρ and ρ^* (or $\rho^\diamond$) are small on the lateral surface, so results from the density and the pressure formulations are almost identical.

Figure 5 shows sound spectra for the heated simulation S2, calculated using a FWH surface with the outflow disk included. In this case, improvement from the use of a pressure form of the FWH equation is substantial. The over-prediction at low frequencies is significantly reduced, especially at downstream angles. Differences are limited to low

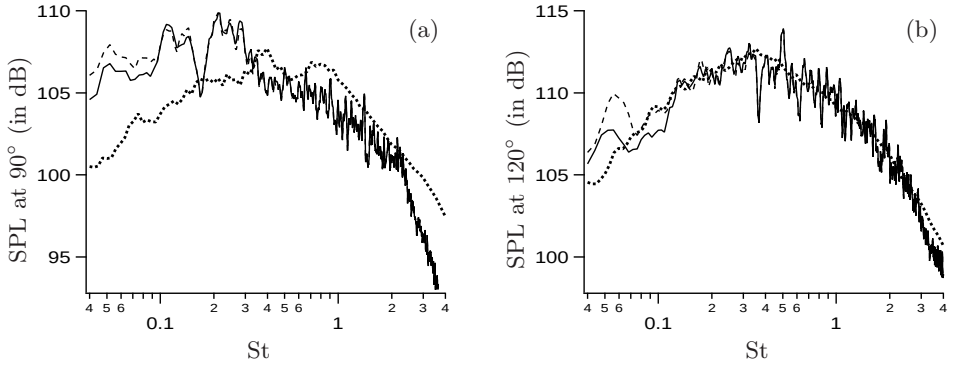

FIGURE 4. Sound pressure level at 90° (a) and 120° (b) for simulation S1 (unheated) calculated with the density formulation (– – – –) and the pressure formulations (———). The outflow disk of the FWH surface is located 27.5 D from the nozzle exit. Experimental results are also displayed (▪▪▪▪▪).

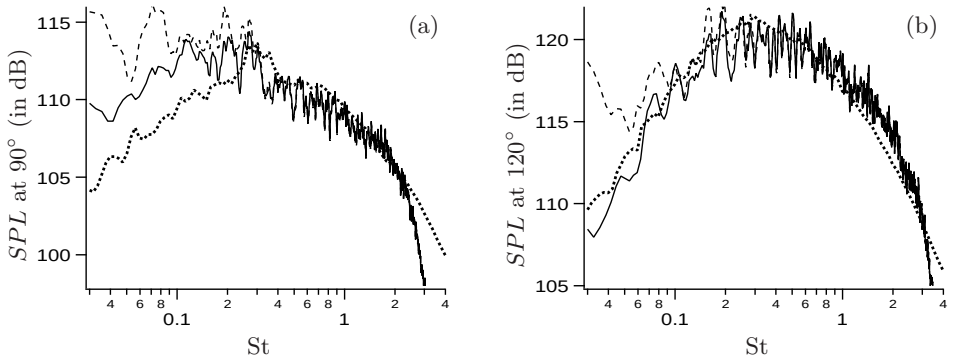

FIGURE 5. Sound pressure level at 90° (a) and 120° (b) for simulation S2 calculated with the density formulation (– – – –) and the pressure formulations (———). The outflow disk of the FWH surface is located 25 D downstream of the nozzle exit. Experimental results are also displayed (▪▪▪▪▪).

frequencies due to the grid stretching in the axial direction: the grid does not sustain high-wavenumber waves at the location of the closing disk.

In conclusion, based on our experience, the pressure-based formulations are better than the original density formulation. All the results obtained concerning the formulations are consistent with the results shown by Spalart and Shur [5].

4.4. FWH surface closure

As stated in the introduction, the question of the downstream end treatment has not been settled, and different studies come to opposite conclusions. The question of how to treat the downstream end of the FWH surface is addressed by comparing results from open or closed surfaces, and using or not outflow disk averaging.

Note first that results using closed surfaces with the outflow disk at different distances from the nozzle exit (25 D, 27.5 D, 30 D, 32.5 D) have been compared, without observing major differences. Turbulent eddies do cross the outflow disks of all these surfaces, but the spurious noise is similar for all these surfaces. Of course, this conclusion would be different if the outflow disks were too close to the nozzle exit.

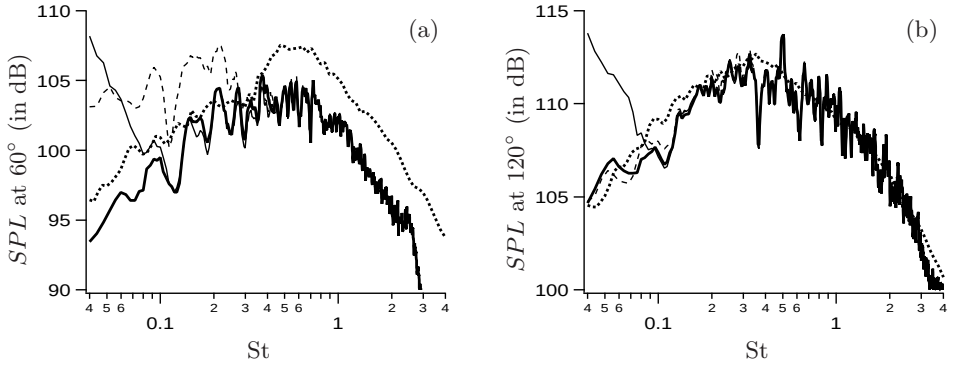

FIGURE 6. Sound pressure level at 60° (a) and 120° (b) for simulation S1 (unheated) changing the outflow disk closure: surface with outflow disk at $x = 30\,D$ (– – – –), same surface without outflow disk (———), and results averaged using 11 surfaces with $\Delta = 0.5\,D$ and $L = 5.0\,D$ (▬▬▬). Experimental results are also displayed (▪▪▪▪▪).

Figure 6 compares the sound spectra obtained from simulation S1, using a pressure formulation, with a closed surface with the outflow disk at $x = 30\,D$, an open surface (the same without outflow disk), and averaging the results from 11 surfaces with their outflow disks located between $x = 25\,D$ and $x = 30\,D$ ($L = 5.0\,D$) and spaced by $\Delta = 0.5\,D$. Note first that the effect of the closure is limited to low frequencies ($St < 0.3$), which depends directly on the grid resolution at the outflow disk location. For both angles considered, results using outflow disk averaging are more accurate. In particular, the experimental shape is recovered. Closed surface results are much noisier at low frequencies for the station located at 60° (Fig. 6a), while they are close to the averaged results at 120° (Fig. 6b). Results using the open surface depart from the averaged results at lower frequency ($St < 0.1$). However, the errors at low frequencies are impressive, and can reach +20 dB for St close to St_{min} [24]. Note that exactly the same types of errors are shown for open surfaces by Shur *et al.* [17], who identified them as pseudo-sound generated by the passage of vortices near the downstream end of the open FWH surface.

The same test has been performed on the heated case S2 with the original formulation (not shown), with exactly the same observations. However, as discussed previously in section 4.3, the formulation has no influence when using open surfaces, whereas the spurious sound obtained using closed surfaces with the original formulation is higher than with a pressure formulation. For hot jets and with the density formulation, open surfaces thus seem better than closed surfaces. Note also that outflow disk averaging is not sufficient to completely correct these errors.

Finally, the same comparison is shown for S2 using a pressure formulation, at four different angles with, again, the same conclusions (Fig. 7). The inaccuracy related to the use of a closed surface decreases with the angle (results with a closed surface are good for $\theta > 90°$). On the contrary, open surfaces show spurious artifacts at all angles, due to truncation error. Closed surfaces yield spurious noise over a frequency range directly related to the grid cut-off frequency at the downstream end of the surface. Interestingly, studies in favor of open surfaces generally use an axial grid stretching that is either less aggressive than in the present study and that of Shur *et al.* [17] or no stretching at all [see for example 11, 15] and the original density formulation. These options maximize the frequency range and the amplitude of the error related to the use of closed surfaces.

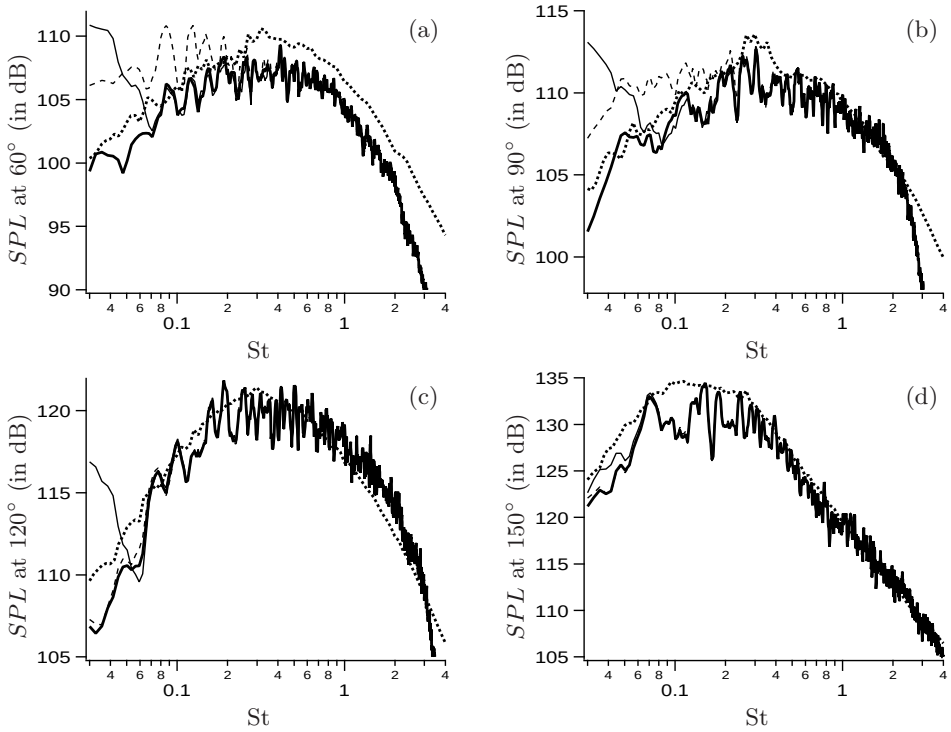

FIGURE 7. Sound pressure level at 60° (a), 90° (b), 120° (c) and 150° (d) for simulation S2 (heated) changing the outflow disk closure: surface with outflow disk at $x = 25\,D$ (– – – –), same surface without outflow disk (———) and results averaged using 11 surfaces with $\Delta = 0.5\,D$ and $L = 5.0\,D$ (▬▬▬). Experimental results are also displayed (▪▪▪▪▪).

4.5. Outflow disk averaging: assessment of spacing and number of disks

From the results shown in the former sections, it is clear that best results are obtained using a pressure-based formulation with outflow disk averaging. The aim is now to clarify how to choose the number of outflow disks for averaging, and the distance between them.

A simple reasoning is used to estimate St_s, the Strouhal number for which outflow disk averaging has maximum effect. Let us consider that the passage of a vortex at time t through an outflow disk is seen by an observer as a spurious acoustic wave that we consider sinusoidal, of period t_s. If this vortex is frozen and convected at the convection speed U_c, it reaches the following outflow disk with the time delay Δ/U_c, where Δ is the streamwise distance between two consecutive outflow disks. When reaching the second outflow disk, the frozen vortex will produce the same sinusoidal spurious wave. Using a far-field hypothesis, the two spurious signals are seen by a far-field observer shifted by the time delay Δ/U_c. In this case, pure cancellation of the two signals occurs if $\Delta/U_c = t_s/2$ ($St_s = U_c\,D/2U_j\,\Delta$). In other words, Δ and L can be chosen by considering that outflow disk averaging will be efficient in the approximate range:

$$\frac{U_c\,D}{2U_j\,L} < St < \frac{U_c\,D}{2U_j\,\Delta} \tag{9}$$

The relevance of this expression is addressed in the following. Figure 8 shows how sound spectra obtained in case S1 by outflow disk averaging vary by changing the distance

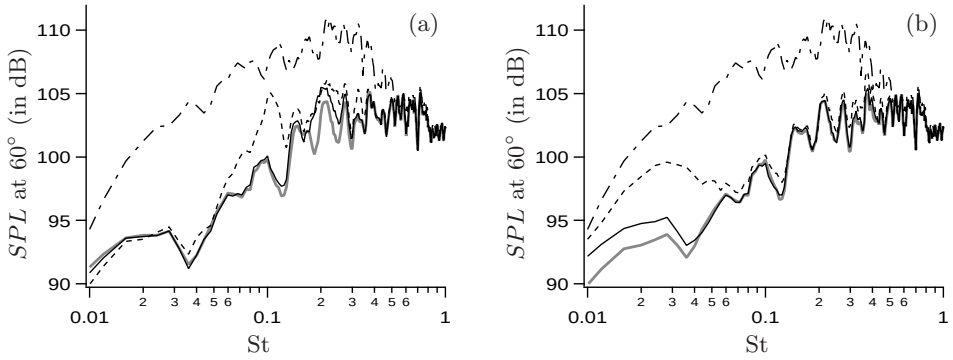

FIGURE 8. Sound pressure level at 60° for simulation S1 (unheated) calculated using outflow disk averaging. (a) $L = 6.0\,D$ and $\Delta = 0.5\,D$ (——), $\Delta = 1.0\,D$ (——) and $\Delta = 2.0\,D$ (– – – –). (b) $\Delta = 0.5\,D$ and $L = 2.5\,D$ (– – – –), $L = 5.0\,D$ (——) and $L = 7.5\,D$ (——). Results from a closed surface with the outflow disk at $x = 25\,D$ (— – —) is shown for a. and b.

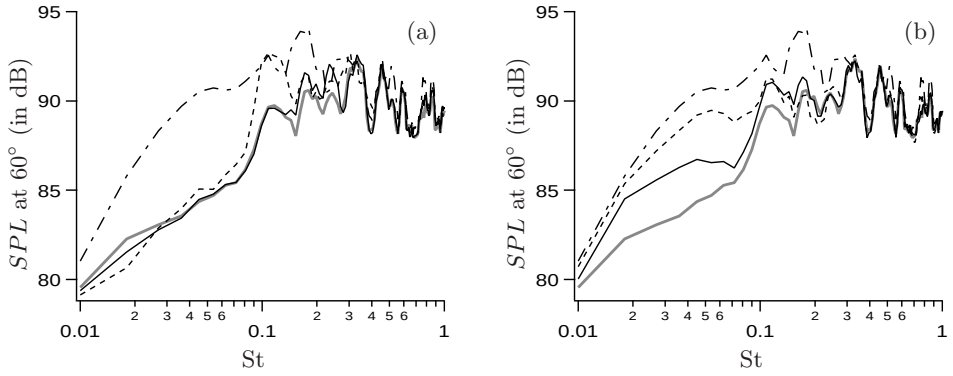

FIGURE 9. Sound pressure level at 60° for the subsonic simulation (cold) calculated using outflow disk averaging. (a) $L = 4.0\,D$ and $\Delta = 0.5\,D$ (——), $\Delta = 1.0\,D$ (——) and $\Delta = 2.0\,D$ (– – – –). (b) $\Delta = 0.5\,D$ and $L = 1.0\,D$ (– – – –), $L = 2.0\,D$ (——) and $L = 4.0\,D$ (——). Results from a closed surface with the outflow disk at $x = 25\,D$ (— – —) is shown for a. and b.

between two consecutive outflow disks, Δ (Fig. 8a), or the distance between the first and the last outflow disks, L (Fig. 8b). An upstream angle (60°) is shown, where the effect of averaging is maximum. In Fig. 8(a), outflow disks are separated by $\Delta = 0.5\,D$, $1.0\,D$, and $2.0\,D$. The first two cases are compared: averaging with $\Delta = 0.5\,D$ or $\Delta = 1.0\,D$ gives very close results, except in the range $0.15 < St < 0.3$. If time-averaged velocity is considered as a good estimate for U_c, then $U_c \approx 0.3U_j$ in S1 in the region where outflow disks are located. With $\Delta = 0.5\,D$, the maximum effect for outflow disk averaging should be seen for $St_s = 0.3$. The simple formula used above gives a good approximation, although high, of the range of maximum effect of averaging. This is also confirmed by comparing the cases where $\Delta = 1.0\,D$ and $\Delta = 2.0\,D$. Maximum efficiency for $\Delta = 1.0\,D$ should be seen around $St_s = 0.15$, and the two cases indeed differ in the range $0.06 < St < 0.15$.

Figure 8(b) shows how results obtained by averaging vary by changing L. When using outflow disk averaging, L appears to determine the low-frequency limit of effectiveness of averaging. Spurious effects are moved down to lower and lower frequencies as L increases. Three cases are compared: $L = 2.5\,D$ ($St_s = 0.06$), $L = 5.0\,D$ ($St_s = 0.03$), and $L = 7.5\,D$

($St_s = 0.02$). Again, the relevance of the formula to evaluate St_s is observed. It is shown in Fig. 8(b) that averaging over surfaces with $L = 5.0\,D$ (resp. $7.5\,D$) mainly reduces the spurious sound around $St = 0.03$ (resp. $St = 0.02$) compared to the case where $L = 2.5\,D$ (resp. $5.0\,D$).

To illustrate the relevance of the formula, a completely different case is shown in Fig. 9, using simulation S3. Noise results are post-processed using outflow disk averaging and the effect of Δ and L is shown in Fig. 9(a) and Fig. 9(b), respectively. In this case, $U_c = 0.3\,U_j$ is a good estimate. Figure 9(a) compares three cases, both with $L = 4.0\,D$: $\Delta = 0.5\,D$, $1.0\,D$, and $2.0\,D$. Case $\Delta = 1.0\,D$ is expected to depart from case $\Delta = 0.5\,D$ around $St_s = 0.3$. Case $\Delta = 2.0\,D$ is expected to depart from case $\Delta = 1.0\,D$ around $St_s = 0.15$. Figure 9 confirms this expectation deduced from Eq. (9), although showing that the estimate is slightly too high. Figure 8(b) shows how results obtained by averaging vary by changing L (with $\Delta = 0.5\,D$). From Eq. (9), maximum efficiency of the averaging is expected for St in the range $[0.15, 0.3]$ for $L = 1.0\,D$, $[0.075, 0.3]$ for $L = 2.0\,D$ and $[0.0375, 0.3]$ for $L = 4.0\,D$. The relevance of Eq. (9) is shown again, this time on a subsonic cold jet.

5. BEST PRACTICE FOR THE USE OF A PERMEABLE-SURFACE FWH SOLVER

The present study was mainly undertaken because of the diversity of results and conclusions in the literature about the usage of a FWH solver. In addition, available publications on the topic rarely provide very practical details, but concentrate on the most fundamental issues. The purpose of this section is to provide a summary of technical tests performed with our FWH solver in order to provide a set of best practices for new users of FWH solvers. Results are either displayed in the present paper or (for more technical results) in a former publication [24].

(*a*) To obtain converged acoustic results for a given frequency f, the time record used for FWH computations has to be at least $10\,f^{-1}$ [24]. In conjunction with this time record, windowing should be used; the Hanning window is used here. It is critical to rescale the signal so that it carries the same energy as the original signal [22].

(*b*) For validation against experimental measurement, numerical noise results should be generated exactly as in reference experiment. Even if perfectly accurate to predict the true far-field noise, far-field assumptions may lead to discrepancies, as experimental data is not always measured in the true far field. Far-field assumptions may also spoil the results if one is interested in low frequencies. In the end, it is advised to conserve the full FWH equations, as the computational time saved omitting the F_2 term is small compared to the total computational time.

(*c*) The pressure-based formulations perform better than the original density-based formulation for FWH predictions with the volume integral omitted. This is due to a decrease of spurious noise generated at the downstream end of the surface. When open surfaces are used, differences between the formulation are small.

(*d*) In conjunction with the FWH equation based on pressure, closed surfaces give better results than open surfaces, in particular for downstream observers. However, spurious noise is still visible for upstream observers. The use of outflow disk averaging significantly decreases this spurious noise and should be used routinely. The combination of pressure-based formulation and outflow disk averaging provides the best results, as they

minimize the error associated with closed surfaces, while avoiding the omission and truncation errors related to open surfaces.

(*e*) The study of outflow disk averaging has shown that the number and the spacing of the outflow disks can be estimated from a simple expression, provided in section 4.5.

(*f*) The question of the location of the FWH surface is crucial: first, it has to be long enough and far enough from the jet axis, to enclose as much as possible the noise sources. In the axial direction, when jets issue in a medium at rest, the surfaces extend until $20\,D \leq x \leq 30\,D$, depending on the studies [5, 15–18, 20]; $25\,D$ is a good estimate of the length of the surface downstream of the nozzle exit. In terms of radial extent, the surface can be far from the jet without any loss of precision only if the grid size is homogeneous. In practice, however, grids are progressively stretched in the radial and axial direction to keep the computational cost manageable. The FWH surface should thus be as close as possible to the jet, so that the grid resolution remain sufficient to propagate the high-frequency acoustic waves accurately. These two conflicting constraints make the FWH results very sensitive to the FWH surface location when stretched grids are used: a tight surface fails to enclose the noise sources, while a loose one induces loss of information for high-frequency waves. To solve this dilemma, it was found that a good solution lied in the grid itself [6, 24]. Radial grid stretching between the edge of the jet and the FWH surface should be kept as moderate as possible, so that the results are less sensitive to the exact location of the surface. This obviously increases the computational cost, but it was found to be legitimate to be able to decide *a priori* where to place the surface without spoiling the noise results.

ACKNOWLEDGMENTS

This work was supported through NASA grant NNX07AC94A. Computations were supported by NSF through TeraGrid resources (project CTS090081) provided by the NICS on the Kraken supercomputer. The authors thank Dr. Bridges and Dr. De Bonis, NASA Glenn Research Center for sharing the experimental database, and Dr. Ham, Dr. Sharma and Dr. Bose (CTR, Stanford) for their help.

APPENDIX: EFFECT OF THE FWH RADIAL LOCATION

To study the effect of surface location, far-field noise is calculated from the S2 simulation, using three different FWH surfaces. The first surface is the one used in the bulk of the paper. It is closed by one outflow disk at $x_{end} = 25\,D$ and its radial location is described by

$$\mathscr{R}(x/D) = 0.75 + 0.1(x/D). \tag{10}$$

The second and the third surfaces differs by their radial location. For the looser surface, $\mathscr{R}'(x/D)$ is defined as:

$$\mathscr{R}'(x/D) = 1.0 + 0.14(x/D). \tag{11}$$

Note that due to radial grid stretching, the grid resolution in the radial direction is approximately twice as coarse at $\mathscr{R}'(x/D)$ that at $\mathscr{R}(x/D)$ near the nozzle exit. For the tight surface, the radial location $\mathscr{R}''(x/D)$ is:

$$\mathscr{R}''(x/D) = \begin{cases} 0.55 + 0.12(x/D) & x/D \leq 5.0 \\ 1.0 + 0.03(x/D) & x/D > 5.0. \end{cases} \tag{12}$$

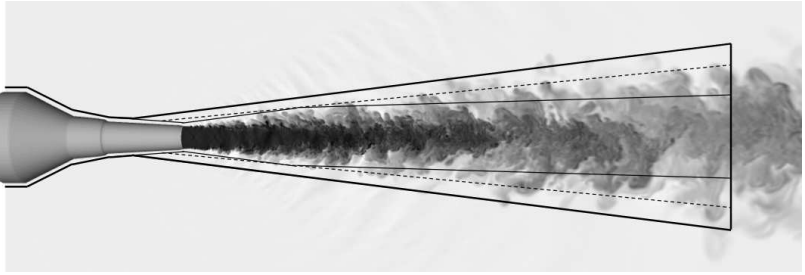

FIGURE 10. Location of the three surfaces used in appendix, superimposed on a density field: $\mathscr{R}$ (– – – –), $\mathscr{R}'$ (▬▬▬) and $\mathscr{R}''$ (———).

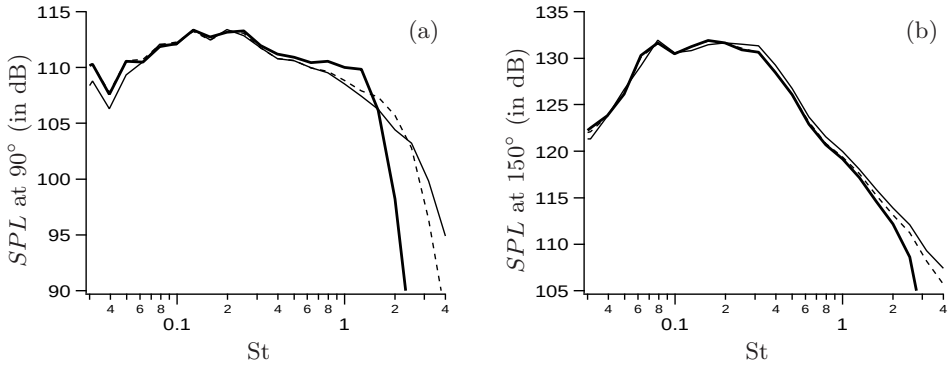

FIGURE 11. Sound pressure level at 90° (a) and 150° (b) for simulation S2 calculated with the reference surface $\mathscr{R}$ (– – – –), the loose surface $\mathscr{R}'$ (▬▬▬), and the tight surface $\mathscr{R}''$ (———).

Locations of the surfaces are displayed on a view of the density field over the symmetry plane (Fig. 10). The loose surface is almost never touched by the turbulent eddies, while the tight surface clearly lies in the turbulent zone downstream of $x = 5\,D$.

A pressure form of the FWH is used to compute far-field sound using Hanning-windowed data recorded over each surface. Figure 11 shows the comparison for two observer angles, but conclusions drawn from these results are valid for all observer locations.

For Strouhal numbers lower than 0.5, no major difference is seen between the calculations. At very low frequencies, the tight surface fails to enclose the noise sources entirely, but underestimation of the low-frequency noise is moderate (less than 2 dB). Larger differences are observed for $St > 0.5$ As the surface described by $\mathscr{R}'$ lies in a region of lower grid resolution, the grid cut-off Strouhal number is lower: short-wavelength acoustic waves are not sufficiently resolved by the LES grid: for $St > 1.5$, SPL drops rapidly when using a loose surface. Note that the LES scheme used has been previously shown to be essentially dispersive at high wave-numbers [6] resulting in high-frequency sound aliased to lower-frequency noise. As a consequence, under-resolution of sound waves yields an increase in noise for $0.5 < St < 1.5$ using $\mathscr{R}'$ instead of $\mathscr{R}$. The effect is larger for sideline angles (Fig. 11a) than for downstream shallow angles (Fig. 11b), for which axial resolution is more involved. The same differences, though less pronounced, are observed at higher frequencies when comparing the results obtained with reference surface $\mathscr{R}$ and with the tight surface $\mathscr{R}''$. Additional discussion about grid resolution at the location of the FWH surface is provided in refs. [6] and [24].

References

[1] Bodony, D. J. and Lele, S. K., "Current Status of Jet Noise Predictions Using Large-Eddy Simulation," *AIAA J.*, Vol. 46, No. 3, 2008, pp. 364–380.

[2] Bogey, C., Barré, S., and Bailly, C., "Direct computation of the noise generated by subsonic jets originating from a straight pipe nozzle," *Int. J. Aeroacous.*, Vol. 7, No. 1, 2008, pp. 1–22.

[3] Bogey, C. and Bailly, C., "Influence of nozzle-exit boundary-layer conditions on the flow and acoustic fields of initially laminar jets," *J. Fluid Mech.*, Vol. 663, 2010, pp. 507–538.

[4] Karabasov, S. A., Afsar, M. Z., Hynes, T. P., Dowling, A. P., McMullan, W. A., Pokora, C. D., Page, G. J., and McGuirk, J. J., "Jet Noise: Acoustic Analogy Informed by Large Eddy Simulation," *AIAA J.*, Vol. 48, No. 7, 2010, pp. 1312–1325.

[5] Spalart, P. R. and Shur, M. L., "Variants of the Ffowcs Williams–Hawkings equation and their coupling with simulations of hot jets," *Int. J. Aeroacous.*, Vol. 8, No. 5, 2009, pp. 477–492.

[6] Mendez, S., Shoeybi, M., Sharma, A., Ham, F. E., Lele, S. K., and Moin, P., "Large-Eddy Simulations of Perfectly Expanded Supersonic Jets Using an Unstructured Solver," *AIAA J.*, Vol. 50, No. 5, 2012, pp. 1103–1118.

[7] Viswanathan, K., Shur, M. L., Spalart, P. R., and Strelets, M. K., "Flow and Noise Predictions for Single and Dual-Stream Beveled Nozzles," *AIAA J.*, Vol. 46, No. 3, 2008, pp. 601–626.

[8] Burak, M. O., Eriksson, L.-E., Munday, D., Gutmark, E., and Prisell, E., "Experimental and Numerical Investigation of a Supersonic C-D Nozzle. AIAA 2009-3252," *15th AIAA/CEAS Aeroacoustics Conference, Miami, Florida, USA, 11-13 May 2009*, 2009.

[9] Lighthill, M. J., "On sound generated aerodynamically : I. General theory," *Proc. R. Soc. Lond. A*, Vol. 211, 1952, pp. 564–581.

[10] Freund, J. B., "Noise sources in a low-Reynolds-number turbulent jet at Mach 0.9," *J. Fluid Mech.*, Vol. 438, 2001, pp. 277–305.

[11] Uzun, A., Lyrintsis, A. S., and Blaisdell, G. A., "Coupling of integral acoustics methods with LES for jet noise prediction," *Int. J. Aeroacous.*, Vol. 3, No. 4, 2004, pp. 297–346.

[12] Goldstein, M. E., "A generalized acoustic analogy," *J. Fluid Mech.*, Vol. 488, 2003, pp. 315–333.

[13] Farassat, F. and Myers, M. K., "Extension of Kirchhoff's formula to radiation from moving surfaces," *J. Sound Vib.*, Vol. 123, No. 3, 1988, pp. 451–460.

[14] Ffowcs Williams, J. E. and Hawkings, D. L., "Sound generation by turbulence and surface in arbitrary motion," *Phil. Trans. R. Soc. Lond. A*, Vol. 264, 1969, pp. 321–342.

[15] Rahier, G., Prieur, J., Vuillot, F., Lupoglazoff, N., and Biancherin, A., "Investigation of integral surface formulations for acoustic predictions of hot jets starting from unsteady aerodynamic simulations. AIAA 2003-3164," *9th AIAA/CEAS Aeroacoustics Conference, Hilton Head, South Carolina, May 12-14, 2003*, 2003.

[16] Eastwood, S., Tucker, P., and Xia, H., "High-Performance Computing in Jet Aerodynamics," *Parallel Scientific Computing and Optimization*, edited by S. N. York, Vol. 27 of *Springer Optimization and Its Applications*, 2009, pp. 193–206.

[17] Shur, M. L., Spalart, P. R., and Strelets, M. K., "Noise prediction for increasingly complex jets. Part I: Methods and tests," *Int. J. Aeroacous.*, Vol. 4, No. 3&4, 2005,

pp. 213–246.

[18] Bodard, G., Bailly, C., and Vuillot, F., "Matched hybrid approaches to predict jet noise by using Large-Eddy Simulation. AIAA 2009-3316," *15th AIAA/CEAS Aeroacoustics Conference, Miami, Florida, USA, 11-13 May 2009*, 2009.

[19] Bodony, D. J. and Lele, S. K., "On using large-eddy simulation for the prediction of noise from cold and heated turbulent jets," *Phys. Fluids*, Vol. 17, 2005.

[20] Paliath, U. and Morris, P. J., "Prediction of Jet Noise From Circular Beveled Nozzles, AIAA 2005-3096," *11th AIAA-CEAS Aeroacoustics Conference, Monterey, California, May 23-25, 2005*, 2005.

[21] di Francescantonio, P., "A new boundary integral formulation for the prediction of sound radiation," *J. Sound Vib.*, Vol. 202, No. 4, 1997, pp. 491–509.

[22] Shoeybi, M., *A hybrid implicit-explicit method for the LES of compressible flows on unstructured grids*, Ph.D. thesis, Department of Mechanical Engineering. Stanford University, 2010.

[23] Morfey, C. L. and Wright, M. C. M., "Extensions of Lighthill's acoustic analogy with application to computational aeroacoustics," *Proc. R. Soc. Lond. A*, Vol. 463, 2007, pp. 2101–2127.

[24] Mendez, S., Sharma, A., Shoeybi, M., and Lele, S. K., "Post-processing of large-eddy simulations for jet noise predictions," *Annual Research Briefs*, 2009.

[25] Shoeybi, M., Svärd, M., Ham, F. E., and Moin, P., "An adaptive implicit–explicit scheme for the DNS and LES of compressible flows on unstructured grids," *J. Comput. Phys.*, Vol. 229, No. 17, 2010, pp. 5944–5965.

[26] Moin, P., Squires, K., Cabot, W., and Lee, S., "A dynamic subgrid-scale model for compressible turbulence and scalar transport," *Phys. FluidsA*, Vol. 3, No. 11, 1991, pp. 2746–2757.

[27] Lilly, D. K., "A proposed modification of the Germano sub-grid closure method," *Phys. FluidsA*, Vol. 4, No. 3, 1992, pp. 633–635.

[28] Cook, A. W. and Cabot, W. H., "Hyperviscosity for shock-turbulence interactions," *J. Comput. Phys.*, Vol. 203, 2005, pp. 379–385.

[29] Mani, A., Larsson, J., and Moin, P., "Suitability of artificial bulk viscosity for large-eddy simulation of turbulent flows with shocks," *J. Comput. Phys.*, Vol. 228, No. 19, 2009, pp. 7368–7374.

[30] Bridges, J. and Wernet, M. P., "Turbulence Associated with Broadband Shock Noise in Hot Jets, AIAA 2008-2834," *14th AIAA/CEAS Aeroacoustics Conference, Vancouver, CANADA, 5-7 May 2008*, 2008.

[31] Ham, F. E., Sharma, A., Shoeybi, M., Lele, S. K., and Moin, P., "Noise Prediction from Cold High-Speed Turbulent Jets Using Large-Eddy Simulation. AIAA 2009-9," *47th AIAA Aerospace Sciences Meeting Including The New Horizons Forum and Aerospace Exposition, Orlando, Florida, 5-8 January 2009*, 2009.